Optics Letters

Dual-polarized transmissive metasurfaces for near-unitary-NA analog spatial computing empowered by impedance matching and mismatching

Yongliang Liu,[1] Wenwei Liu,[1,4] Qi Liu,[1] Yifei Xu,[1] Bo Yu,[1] Zhancheng Li,[1] Hua Cheng,[1,5] and Shuqi Chen[1,2,3,*]

[1]The Key Laboratory of Weak Light Nonlinear Photonics, Ministry of Education, School of Physics and TEDA Institute of Applied Physics, Nankai University, Tianjin 300071, China
[2]School of Materials Science and Engineering, Smart Sensing Interdisciplinary Science Center, Nankai University, Tianjin 300350, China
[3]The Collaborative Innovation Center of Extreme Optics, Shanxi University, Taiyuan 030006, China
[4]wliu@nankai.edu.cn
[5]hcheng@nankai.edu.cn
*schen@nankai.edu.cn

Received 16 July 2024; revised 14 August 2024; accepted 15 August 2024; posted 15 August 2024; published 26 August 2024

In recent years, due to the increasing requirement for real-time and massive data processing, optical analog computation has arisen as a promising alternative to digital computation. Optical spatial differentiation plays a fundamentally important role in various emerging technologies, including augmented reality, autonomous driving, and object recognition. However, previous demonstrations encountered several limitations, such as the dependence on polarization states and a typically limited numerical aperture (NA) of about 0.5, especially in the transmission mode. Here, a new, to our knowledge, design strategy based on the evolution between impedance matching and mismatching in a metasurface is proposed to fill this gap, which can perform dual-polarized second-order derivative for image processing. Our scheme enables high transmission under dual polarization over an 85° incident angle range (NA = 0.996), resulting in more than twofold spatial resolution. Our work paves the way for polarization-insensitive high-resolution signal and image processing in the terahertz region.

https://doi.org/10.1364/OL.536788

Fundamental mathematical operations are ubiquitous to describe any physical system, and a physical system in return can be employed to perform mathematical operations and signal processing [1]. With the increasing demand for real-time, massive data processing, integrated circuits are rapidly reaching the limits of Moore's law. As a result, relying solely on traditional technology struggles to keep up with the growing need for compact, highly parallel, and energy-efficient devices. These limitations, along with the rapidly growing demand for data processing, have strengthened the interest in analog optical computing for performing mathematical operations and image processing, considering the intrinsic parallel processing capacity and high speed of photons [2]. Recently, researchers have developed high-performance optical computing devices for the required signal processing tasks, which have become one of the focuses in information processing [3]. According to Fourier optics, a 4f optical filtering setup consisting of two optical lenses and a filter can be employed for analog image differentiation, whereas such optical systems are rather bulky and difficult to implement for compact integration and minimization.

In recent years, optical analog computing achieved by metasurfaces has provided a new possibility for ultrahigh-speed and massive data analog optical processors. By manipulating the incidence-angle-dependent optical responses, metasurfaces can realize effective filtering of angular optical fields in momentum space on a compact size, which can further be applied for optical data processing. This method has already been successfully implemented for various analog optical devices such as differentiators [4], integrators, and equation solvers. Specifically, optical differentiation has been theoretically and experimentally demonstrated based on various strategies such as surface plasmon polariton (SPP), Brewster's effect, and bound state in the continuum [5,6]. However, these approaches have certain limitations; e.g., almost all SPP schemes are limited in the reflection mode or resulting in low numerical aperture (NA) or polarization independent due to the restricted optical response of the metasurface structure under oblique incidence. Generally, optical media exhibit greater transmittance at smaller incident angles and near unitary reflectance as the angle approaches 90°. To realize antireflection at large angles, all-dielectric multilayer films can be used due to the multiple interference phenomena according to the transfer matrix formula [7,8]. Antireflection across ultrawide-angle has been realized by individual modulation for different incident angles based on metasurfaces in the microwave band [9]. Nonetheless, achieving tailored transmittance over a large angular range remains challenging. To date,

Corrected 3 September 2024

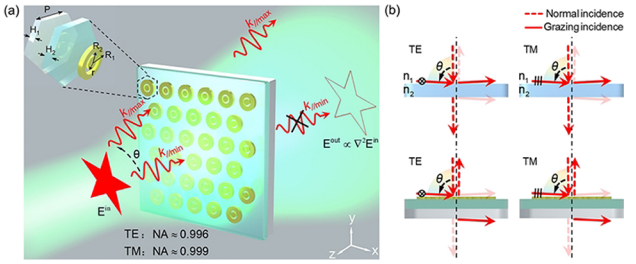

Fig. 1. (a) Schematic of using metasurface to implement the differentiation operation on an input image. $k_{//\max}$ represents the largest parallel wave vector in the Fourier decomposition of the image. (b) Transmission and reflection of multi-angle incident light through conventional transmissive interfaces and the metasurface. The gradation of the colored arrows represents the intensity of light.

achieving ultrahigh-NA transmissive edge detection operating in dual-polarized modes is still highly demanding.

Here, we propose a near-unitary-NA metasurface for analog optical spatial computing operating in both transverse-electric (TE) and transverse-magnetic (TM) transmissive polarized modes. Our scheme realizes second-order derivative on the incident light fields based on the strategy of impedance matching and mismatching in the momentum space, which enables 0.963 (0.76) transmission of light reaching a grazing incident angle of 89° (85°) for TM (TE) polarization. The high NA metasurface significantly increases the highest spatial resolution to be handled by the metasurface and achieves dual-polarized isotropic edge detection. Our approach provides a new strategy for high-performance edge detection and benefits various applications such as artificial intelligence recognition and ultrafast mathematical operations.

A schematic of the spatial second-order differentiator is shown in Fig. 1. The proposed metasurface consists of gold artificial structures and a polyimide (PI) layer on a parylene C substrate. The metasurface can transform an image (E^{in}) into its spatial second-order derivative ($E^{\text{out}} \propto \nabla^2 E^{\text{in}}$), enabling direct edge detection of an arbitrary incident image. To obtain the image edge information in 2 dimensions (2D) for light incident along the z-direction, an isotropic transfer function follows the function [10]:

$$t(k_x, k_y) = \begin{pmatrix} \alpha_s({k_x}^2 + {k_y}^2) & 0 \\ 0 & \alpha_p({k_x}^2 + {k_y}^2) \end{pmatrix}, \quad (1)$$

where k_x and k_y represent the wave vectors along the x- and y-directions; α_s and α_p correspond to the transmission coefficient of the TE- and TM-polarized light. To accomplish the second-order derivative, the transfer function requires efficient and quadratical filtering of the spatial frequency.

To identify the overall edge information of E^{in}, the $\text{NA} = n\sin(\theta_{\max})$ ($n = 1$ in free space, θ is the oblique angle of the incident light) of the metasurface must satisfy $\text{NA} \geq k_{//\max}/k_0$ [11]. To realize the desired optical transfer function (OTF) working till the grazing angles, we propose a metasurface with the unit cell consisting of Au artificial structures with thickness of 0.2 μm and a PI layer ($H_1 = 20$ μm) on a parylene C film ($H_2 = 20$ μm), as shown in Fig. 1(a). The edge length (P) of the hexagon unit cell is 30 μm. The structural parameters of the metallic meta-structures are: $R_1 = 17.5$ μm, $R_2 = 12.5$ μm, and $r = 7$ μm. The simulated structural tolerance of the metallic structures is about 1 μm. The corresponding NAs are 0.996 and 0.999 under the TE and TM polarization, respectively. As

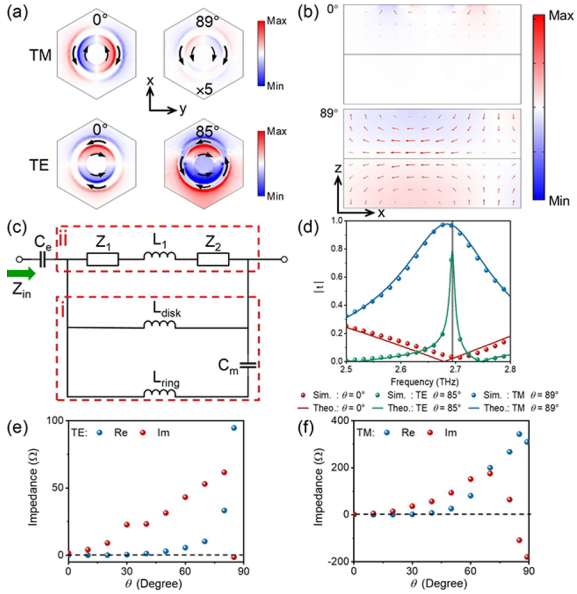

Fig. 2. (a) Near-field H_z distributions on the metasurface with different incident angles and polarizations at 2.694 THz. The black arrows indicate the distribution of surface currents. (b) Displacement current distribution in the cross section (y–z) of two dielectric films for TM-polarized waves. (c) Transformed equivalent circuit model of the proposed metasurface. The red dashed boxes represent the equivalent circuit corresponding to metallic structures (i) and bilayer films (ii). (d) Theoretical and simulated transmission spectra with different incident angles. The gray line denotes the operating frequency. Retrieved equivalent impedance with different incident angles for (e) TE polarization and (f) TM polarization. The zero impedance is denoted by the black dashed line for comparison.

shown in Fig. 1(b), when light encounters a transmissive boundary between two media with different refractive indices, high transmission decided by the index contrast is usually anticipated under normal incidence; whereas high reflection exists for any conventional media under the grazing incidence [12]. Interestingly, our design reverses such phenomena based on the impedance matching and mismatching strategy.

To reveal the underlying physics, we simulated the distributions of near-field H_z with different incident angles under different polarizations, as shown in Fig. 2(a). At normal incidence, the generated opposite currents within two meta-structures lead to not only the reduction of dipole responses but also a π-phase difference of the magnetic components in different regions, resulting in a significantly diminished far-field emission [13]. For the grazing incidence such as $\theta = 89°$ under TM polarization, the currents on the metallic structures can be treated as a pair of parallel dipoles to form a symmetric resonant mode, which cooperatively contribute to the enhanced transmission. In comparison, the distributions of current flows and near-field H_z on the central disk for $\theta = 85°$ are almost the same under TE polarization, while the current distribution on the metallic ring has changed. The equivalent inductance and capacitance originate from the generation of currents and the accumulation of charges following the interaction between electromagnetic waves and the structure. Based on the transmission line theory, such variations of surface currents can be characterized by the equivalent circuit model that undergoes varied inductances and the capacitive coupling [14–16] [Fig. 2(c)]. To

determine the type of the electrical components, we first simulated the electromagnetic responses of metasurfaces including electromagnetic fields and surface currents. It is worth noting that we employ a double-layered substrate to modulate the near fields and induce displacement currents, as shown in the y–z cross section of two dielectric films in Fig. 2(b). According to the Ampère–Maxwell law, the varying displacement current loop induces a varied magnetic field, which can be characterized in terms of an equivalent inductance (L_1) in addition to the intrinsic impedances Z_1 and Z_2 of the two dielectric layers [17]. Compared with the normal incidence, the displacement current loop is stronger at an incidence angle 89°, resulting in an increased inductance (L_1). The capacitance C_m represents the capacitive coupling between the metallic structures [18]. The gap between two adjacent unit cells behaves as capacitive (C_e) under the excitation of the electric fields, as shown in the equivalent circuit model in Fig. 2(c). The effective inductance (L_{ring} for the metallic ring) and capacitances (C_e) can be estimated by the method introduced in Ref. [19,20] with $L_{ring} = l/\lambda^*[ln(\csc(\pi w/p))+G]$ and $C_e = \pi\varepsilon_0 l/ln[(p-w)/t]$, where l is the outer diameter of the ring, w is the effective length, and p is the period of the unit cell. $L_{disk} = w/\alpha\varepsilon_0\omega_p^2 lt$ and $C_m = w\varepsilon_0 t/h$ can also be obtained, where ω_p is the plasma frequency, t is the metal thickness, ε_0 is the permittivity of vacuum, α is the effective factor related to the specific resonant mode, and h is the distance between the metallic ring and the metallic disk. Since the exact effective electrical values of the structures are also decided by the distributed surface currents on the metasurface, the geometric parameters of the artificial structures should be further optimized near the theoretical values to compensate this effect. The exact value of the elements in the circuit model is further retrieved using the software Advanced Design System [21]. Accordingly, the effective impedance of the metallic structures (Z_i), the bilayer film (Z_{ii}) and the total effective impedance (Z) can be obtained as $Z_i = j\omega L_{disk}//(j\omega L_{ring} - j/\omega C_m)$, $Z_{ii} = Z_1 + Z_2 + j\omega L_1$, $Z = Z_i//Z_{ii} - j/\omega C_e$, where ω is the incident angular frequency, // indicates parallel connection. The reflection coefficient (Γ) can be described as follows:

$$\Gamma = \frac{Z_{in} - Z_0}{Z_{in} + Z_0}, \tag{2}$$

where $Z_0 = 377\,\Omega$ is the intrinsic impedance of free space. The transmittance reaches its maximum when the effective impedance of the metasurface matches that of the vacuum ($Z_{in} \approx Z_0$). Through the ongoing optimization of structural parameters, followed by the formulas to compute the parameters of the equivalent components, the target impedance is ultimately achieved. The transmission spectra of the equivalent circuit are consistent with those of the electromagnetic full-wave simulation for both normal and oblique incidences, confirming the validity of the equivalent circuit model [Fig. 2(d)]. We calculated the equivalent impedance of the metasurface with different incident angles [Figs. 2(e) and 2(f)]. The calculated input impedance (Z_{in}) of the metasurface at normal incidence approach 0 Ω, which features a low transmission dip at the operational frequency [Figs. 2(d)] due to the significant impedance mismatching with Z_0. When increasing the incident angle, the effective impedance also increases to 94-$j\times$1.396 Ω and 309.5-$j\times$179.8 Ω for $\theta_{TE} = 85°$ and $\theta_{TM} = 89°$, respectively. Such an approach to the impedance of free space (377 Ω) significantly reduces the reflectivity even at the grazing incidence [Figs. 3(a) and 3(b)]. As a result, the transmission is enhanced

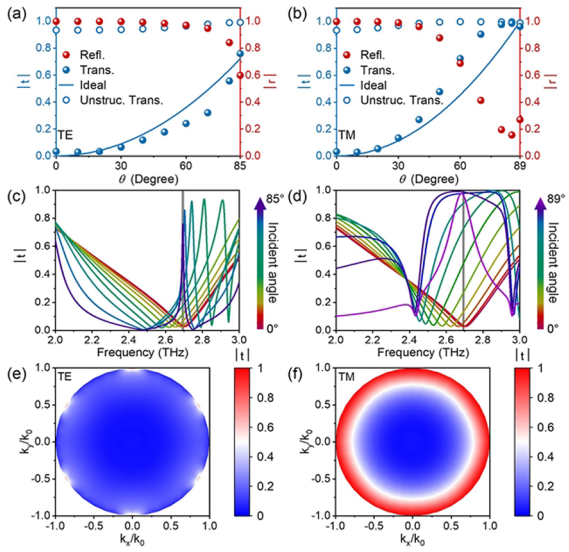

Fig. 3. Calculated (a) and (b) angular and (c) and (d) spectral transmission/reflection amplitudes for (a) and (c) TE and (b) and (d) TM polarization, in comparison with the unstructured doublet film. The gray line denotes the operating frequency. Amplitudes of (e) TE- and (f) TM-polarized 2D transfer functions of the metasurface, showing a corresponding near-unitary transmission.

for extremely large incident angles. Although the theoretical effective impedance obtained from the equivalent circuit model is not exactly the same as that of the free space, the effect of impedance matching is obvious considering the reflectivity is not linearly dependent on the impedance as indicated in Eq. (2). Note that the extremely grazing transmission in both polarization states is challenging with reported results [22], which is the basis to realize near-unitary-NA analog spatial computing combining with low transmission under the normal incidence. Moreover, the transmittance amplitude of the metasurface basically satisfies the quadratic function, which can be used to achieve the second-order derivative on the impingement according to Eq. (1). The transmittance spectra for both TE and TM polarization under various incident angles were simulated for the azimuthal angle $\varphi = 0$ [Figs. 3(c) and 3(d)]. The transmission spectra are the same for both polarization under the normal incidence due to the symmetry of the meta-structure. Whereas for the oblique incidence the resonance dip undergoes a gradual redshift, and the transmittance starts to increase with the increase of the incidence angles at the operating wavelength. This phenomenon is essential for achieving the differential operation. The transmittance changes from approximately zero at normal incident to about 0.76 ($\theta_{TE} = 85°$) and 0.963 ($\theta_{TM} = 89°$). The 2D transfer functions of the metasurface for both TE and TM polarization are further simulated in Figs. 3(e) and 3(f). Although the 2D optical transfer function of the metasurface is anisotropic for TE waves [Fig. 3(e)], it still enables effective edge detection for 2D images, which can be seen from the edge imaging in the following discussion. In comparison, Fig. 3(f) shows that the metasurface exhibits excellent isotropic response in the TM mode. The insensitivity to arbitrary azimuthal angles under TM polarization imparts a robust behavior that the low-frequency wave component of the incident light is effectively impeded, while concurrently allowing the transmission of the high-frequency wave component across in any direction as the incident angle changes from −89° to 89°, thus realizing high

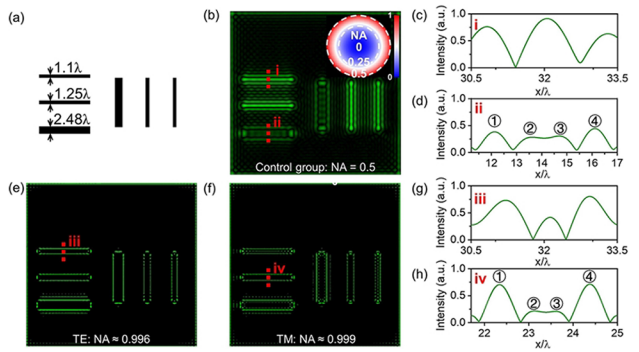

Fig. 4. (a) Mask of the input object to be edge-detected with different widths. (b) Calculated isotropic second-order derivative of the image using a device with a typical NA of 0.5. Inset: the corresponding ideal 2D optical transfer function. (c) and (d) Vertical cuts (i and ii) of the intensity distribution in (b). Calculated (e) TE- and (f) TM-polarized 2D edge detection for the proposed metasurface. (g) and (h) Vertical cuts (iii and iv) of the intensity distribution in (e) and (f).

spatial resolution at the wavelength scale. To analyze the spatial resolution of edge imaging, the rectangular masks with different widths serve as objects to be edge-detected [Fig. 4(a)]. We theoretically investigate the edge imaging properties for an ideal isotropic second-order differentiator with a typical NA of 0.5 to compare with our design, as shown in Fig. 4(b). The inset represents the ideal isotropic 2D transfer function. It can be seen that the control group suffers from broadened edges and limited resolution at the wavelength scale, even though the 2D transfer function is ideal. Figures 4(c) and 4(d) represent the vertical-cut intensity along the red dashed line in Fig. 4(b). Note that the resolution of edge identification is different from the famous Rayleigh diffraction limit 0.61λ/NA defined as the resolvable distance between two Airy disks. The resolution in edge imaging is decided by the resolvable distance between two closely aligned edges. Generally, each edge to be detected corresponds to two peaks after being processed by the second-order derivative metasurface [23]. This phenomenon occurs due to the varying concavity and convexity on opposite sides of the intensity abrupt (positive and negative second-order derivative). When the linewidth of the mask is small enough, the central two peaks merge into a single peak with the intensity much higher than the other two, leading to indiscernible edges, as shown in Fig. 4(c). The central two peaks can be critically identified for a linewidth of 2.48λ, which is the spatial resolution for the 0.5 NA metasurface [Fig. 4(d)]. The two peaks ① and ② correspond to the upper edge of the mask, and the two peaks ③ and ④ correspond to the lower edge. In contrast, our near-unitary-NA metasurface demonstrates notable ability to capture the finer details of mask edges and can effectively enhance high-frequency spatial components under different polarizations [Figs. 4(e)–4(h)]. The slight sidelobe for the 1.1λ-mask in Fig. 4(f) results from the slightly greater deviation from the ideal OTF for the TM polarization. According to the abovementioned criteria, the spatial resolutions for the TE and TM modes are 1.1λ and 1.25λ, respectively, which basically doubles that in the control group with an NA of 0.5. The significantly improved edge detection results from the strategy of impedance matching and mismatching of the ultrahigh-NA metasurface and the quasi-parabolic profile in transmittance in both TE and TM modes. Since the transmittance is a trade-off among the operating NAs and polarization modes, the slight reduction in spatial resolution for the TM mode is observed, which arises from the deviations of the transmittance from the theoretical parabolic value compared with that for the TE mode [Figs. 3(a) and 3(b)].

In conclusion, the spatial modulated metasurface introduced in this study enables the optical transfer function to meet the quadratic dependence on the incoming angular dispersion, which performs dual-polarized second-order derivative with near-unitary NA. The ultrahigh NA helps to capture a greater amount of information from the incident light, which enables achieving high spatial resolution at the wavelength scale. Compared with previous work on transmissive optical computing, the maximum incident angle has been widely extended to above 85°, facilitating high-resolution edge imaging with a spatial resolution limit of 1.1λ (TE) and 1.25λ (TM). Meanwhile, such flexibility of the metasurface can be well integrated with existing systems to enable efficient data processing, which opens up opportunities for terahertz information processing applications, including autonomous driving, machine vision, and biomedical imaging.

Funding. National Key Research and Development Program of China (2021YFA1400601, 2022YFA1404501); National Natural Science Fund for Distinguished Young Scholar (11925403); National Natural Science Foundation of China (12122406, 12192253, 12274237, 12274239, U22A20258); Natural Science Foundation of Tianjin Municipality (22JCYBJC00800, 22JCYBJC01350, 22JCZDJC00400).

Disclosures. The authors declare no conflicts of interest.

Data availability. The data that support the findings of this study are available from the authors upon reasonable request.

REFERENCES

1. M. Moeini and D. L. Sounas, Optica **7**, 1325 (2020).
2. A. Silva, F. Monticone, G. Castaldi, *et al.*, Science **343**, 160 (2014).
3. M. Deng, M. Cotrufo, J. Wang, *et al.*, Nat. Commun. **15**, 2237 (2024).
4. A. Cordaro, H. Kwon, D. Sounas, *et al.*, Nano Lett. **19**, 8418 (2019).
5. C. Zhou, Y. Chen, Y. Li, *et al.*, Adv. Funct. Mater. **34**, 2313777 (2024).
6. Y. Zhou, J. Zhan, Z. Xu, *et al.*, Laser Photonics Rev. **17**, 2300182 (2023).
7. C. Dai, Z. Li, Y. Shi, *et al.*, Laser Photonics Rev. **17**, 2200368 (2023).
8. C. Jin and Y. Yang, Nanophotonics **10**, 3519 (2021).
9. Z. Zhang, Z. Che, J. Chen, *et al.*, Opt. Express **30**, 14002 (2022).
10. Y. Zhou, H. Zheng, I. I. Kravchenko, *et al.*, Nat. Photonics **14**, 316 (2020).
11. H. Kwon, D. Sounas, A. Cordaro, *et al.*, Phys. Rev. Lett. **121**, 173004 (2018).
12. B. E. A. Saleh and M. C. Teich, *Fundamentals of Photonics* (John Wiley & Sons, 2019).
13. J. Cheng, Z. Li, D. Choi, *et al.*, Adv. Opt. Mater. **11**, 2202329 (2023).
14. Y.-C. Chung, K.-W. Lee, I.-P. Hong, *et al.*, IEICE Electron. Express **8**, 89 (2011).
15. C. Huang, B. Zhao, J. Song, *et al.*, IEEE Trans. Antennas Propag. **69**, 3593 (2021).
16. N. M. Estakhri and A. Alù, Phys. Rev. X **6**, 041008 (2016).
17. L. Chen, S.-W. Qu, B.-J. Chen, *et al.*, IEEE Trans. Antennas Propag. **65**, 234 (2017).
18. Y. Wei, J. Duan, H. Jing, *et al.*, IEEEE Trans. Microw. Theory **70**, 2861 (2022).
19. L. Li, L. Ma, H. Sun, *et al.*, ACS Photonics **10**, 2746 (2023).
20. R. J. Langley and E. A. Parker, Electron. Lett. **18**, 294 (1982).
21. Y. Li, P-F. Gu, Z. He, *et al.*, IEEE Trans. Antennas Propag. **70**, 11911 (2022).
22. M. Cotrufo, S. Singh, A. Arora, *et al.*, Optica **10**, 1331 (2023).
23. Y. Liu, M. Huang, Q. Chen, *et al.*, Nat. Commun. **13**, 7944 (2022).